TRANSFER-MATRIX ABSTRACTIONS TO ANALYZE THE EFFECT OF MANUFACTURING VARIATIONS IN SILICON PHOTONIC CIRCUITS

Pratishtha Agnihotri, Priyank Kalla, Steve Blair
Electrical & Computer Engineering, University of Utah
pratishtha.agnihotri@utah.edu, kalla@ece.utah.edu, blair@ece.utah.edu

***Abstract*—The emergence of Silicon (Si) photonics necessitates the development of automated testing and validation techniques. Si-photonic device operation is sensitive to variations in the manufacturing process. This paper describes a methodology and abstraction models to evaluate the effect of variations in the dimensions of waveguides, spacing and modulation parameters on Si-photonic circuits. Such variations may result in signal degradation and phase mismatch, causing interference based devices to operate imperfectly. Experiments are performed on various (linear) optical devices by introducing geometric and layout deformities, and compact models are abstracted in terms of Transfer Matrices. Using these models, we show how the impact of design or manufacturing variations in a device can be analyzed on the operation of optical logic circuits that integrate various such components. The method is validated by experiments performed on conventional SOI waveguide based devices and circuits.**

***Index Terms*—Silicon photonics, manufacturing variations, transfer matrix**

I. INTRODUCTION

Photonics have widespread applications in fields such as communication, signal processing, quantum and reversible computation [1]–[3], optical neural networks [4], optical computing applications such as optical logic and networks-on-chip [1], [5], [6], etc. Though the compatibility with the existing CMOS infrastructure has scaled optoelectronic integrated circuit (OEIC) fabrication to a large extent [7], efforts are needed to develop defect models, test and validation procedures.

Silicon photonic device operation is sensitive to variations in the manufacturing process. Imperfections in optical lithography processes lead to variations in device geometry and layout. Such variations impact spacing between waveguides and modulation parameters during fabrication, which affects the effective refractive index n of waveguides and devices. Refractive index changes affect the phase ϕ of optical waves in the medium ($\phi \propto \frac{2\pi n}{\lambda}, \lambda =$ wavelength of light) and may shift a device's response off its design parameters, resulting in not just performance degradation but also system failure in the worst case. Therefore, it is desirable to develop defect and fault models as well as analysis procedures that can analyze the effect of design and manufacturing variations on operations of large circuits. Such models and tools may further enable post-fabrication tuning and calibration to improve yield and cost. The effect of design or manufacturing errors can be simulated using various OEIC design tools and numerical computational solvers such as Eigenvalue mode solvers or finite difference time domain (FDTD) solvers, *e.g.* the design and simulation suite provided by ANSYS LUMERICAL [8]. Such techniques and tools are computationally intensive – they can simulate the behavior of individual devices, but are infeasible in analyzing the behaviors of circuits that integrate a larger number and variety of OEICs. There is a need for compact yet accurate modeling for Si-photonic circuit layouts.

Objective and Contributions: This paper proposes a hierarchical approach – along with an abstraction model – to analyze the effect of design errors or manufacturing defects and variations on the performance of optoelectronic components, devices and circuits. The paper focuses on linear optical devices such as Si-waveguides, wave splitters, waveguide couplers, electro-optic phase modulators and Mach-Zehnder interferometers (MZIs). Analytical approximation models are developed for estimating the (normalized) transmission power and phase of signals at circuit outputs. Our models are based on the concept of *transfer matrices* [9]. We show that the conventional transfer matrix models can be augmented to include the effect of arbitrary design errors or manufacturing variations that lead to *deformities* in waveguide geometries.

Using conventional SOI waveguide technology parameters, we design and simulate the performance of aforementioned optoelectronic components. Subsequently, a variety of waveguide deformities are introduced in the components to reflect variations/imperfections in the lithography process. Such deformities include dislocation of Y-junctions, deviation of waveguide coupling lengths and spacing between waveguides, changes in applied voltages to the phase modulators, etc. Further simulations are performed over a wide range of deformities. The observed data is *curve fitted [10] to derive a polynomial function abstraction, mapping the deformity dimensions (length) to output power transmission and phase*. These are used as scaling factors and incorporated in our transfer matrix models for the ideal and deformed components. These are composed (cascaded together) to derive transfer matrices for optical circuits. At the component level, our abstraction model accurately estimates device performance under the introduced defects, as verified by fullscale FDTD simulations. However, the execution time of our model is orders of magnitude faster than FDTD. Moreover, when applied to larger OEIC designs – a case study of an optical digital logic circuit with a deformed MZI is presented – our model predicts degraded signal-to-noise ratio, whereas FDTD simulation for this circuit is computationally infeasible.

This research is funded in part by the US National Science Foundation grant CCF-1911007.

978-1-6654-9962-0/22/$31.00 ©2022 IEEE

Related prior work: With regards to manufacturing test, [11] describes a wafer-level test infrastructure enabling semi-automatic OEIC circuit test. The impact of manufacturing variations on Si-photonic OEICs has been well documented [12]. Nikdast *et al* [13] performed a study of fabrication non-uniformity on si-photonic interconnects. Their work employs a two-variable approach to account only for variations in the top silicon thickness and waveguide width. Recently, Banerjee *et al* [14] study the impact of manufacturing uncertainties on neural network performance. Instead of explicitly analyzing variations in waveguide profiles, they simulate the effect of uncertainties by modeling variations in signal phase. In contrast, we explicitly introduce variations in the geometric profiles of device layouts to simulate a range of deformities induced by variations in the lithography process. Using FDTD simulations on deformed devices, we abstract compact models and integrate them within the transfer matrices to accurately and computationally efficiently estimate OEIC performance.

Paper Organization: The rest of the paper is organized as follows. Section II sets up the preliminary concepts and notations of the Si-photonic design parameters employed in our designs and experiments. Section III describes transfer matrices of elementary devices and computation of the transfer matrices for complex devices. Section IV describes our experiments with deformed devices and the abstraction model incorporated into the transfer matrices. Section V demonstrates application of our methodology to an example optical logic circuit. Section VI concludes the paper.

II. Background

Let us consider an optical wave propagating in the z direction inside a waveguide. A travelling wave is expressed as $\psi(z) = A(z) \cdot \Omega(z) \cdot \mathrm{e}^{-i\beta \cdot z}$,where $A(z)$ is the amplitude, $\Omega(z)$ is the mode field and β the propagation constant of wave. A mode field is the distribution pattern of electric and magnetic field components of the wave. The propagation constant is a measure of change in amplitude and phase experienced by a wave while propagating in a given direction. Silicon waveguide is transparent to telecommunication wavelength range enabling it to guide the transmission of wave in the medium. Silicon and silicon dioxide are ideal for constructing optical waveguides given the large refractive index contrast between the two: silicon has a refractive index of 3.43, while silicon dioxide's is 1.45 as shown. There are 3 types of waveguides, as shown in Fig. 1. The photonic wires and slab/planar waveguides are used mostly for modeling purposes, whereas the ridge waveguide is the most commonly used in silicon photonic circuits, as they offer good mode confinement and low losses. In this work, we utilize the ridge waveguide, with the dimensions shown in Fig. 2. In Fig. 2, refractive index of the medium (Si) is shown as n_f, whereas the bottom and top claddings with n_s, n_c respectively. Typically, wavelengths used for optical transmission are 850nm, 1300nm and 1550nm. For Si and SiO_2, intrinsic absorption losses are negligible at 1550nm. So, in this paper, we focus on transmission in ridge waveguide at 1550nm.

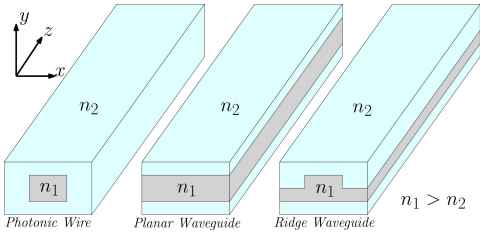

Figure 1: Types of waveguides

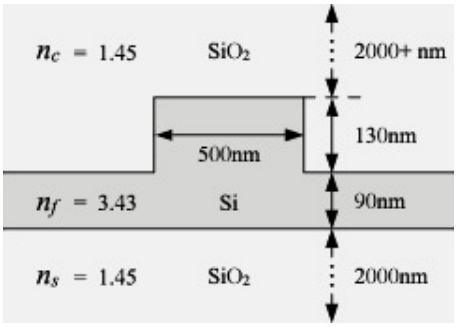

Figure 2: Waveguide profile

III. Transfer Matrices for Optical Systems

Consider an optical system as shown in Fig. 3 consisting of an input ray y_a and angle of incidence θ_a propagating through the system. The optical system performs operations on the input ray. The output ray is y_b with angle θ_b. In the paraxial approximation, when the angles are sufficiently small so that $sin\ \theta = \theta$, the relation between (y_1, θ_1) and (y_2, θ_2) is linear and can be expressed algebraically as follows:

$$\begin{aligned} y_2 &= Ay_1 + B\theta_1 \\ \theta_2 &= Cy_1 + D\theta_1 \end{aligned} \qquad \begin{bmatrix} y_2 \\ \theta_2 \end{bmatrix} = \begin{bmatrix} A & B \\ C & D \end{bmatrix} \cdot \begin{bmatrix} y_1 \\ \theta_1, \end{bmatrix} \quad (1)$$

where A, B, C, and D can be real or complex functions. The matrix in Eqn. (1) is called a *transfer matrix* of the given system. The operations performed by optical devices and systems can be expressed in the form of such a transfer matrix. This concept can be extended to wave optics for analysis of complex optical systems.

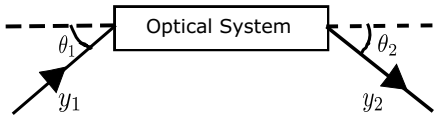

Figure 3: Block diagram of an optical system

A. Transfer matrix for a Beam Splitter

A beam splitter, shown in Fig. 4, has two inputs $\psi_1 = A(z) \cdot \Omega_A(z) \cdot \mathrm{e}^{-i\beta_A z}$ and $\psi_2 = B(z) \cdot \Omega_B(z) \cdot \mathrm{e}^{-i\beta_B z}$, where $\Omega_A(z)$ and $\Omega_B(z)$ are mode fields, $A(z)$, $B(z)$ are amplitudes and β_A, β_B the propagation constants of the input beams, respectively, and z is the direction of propagation. A beam splitter splits the incoming beams into two arms following

amplitude distribution factors α_1 in the upper arm and α_2 in the lower arm. Therefore, the remaining portions of the beams transmitted into upper and lower arm are given by $\alpha_2{}'$ and $\alpha_1{}'$, respectively, following the energy conservation law such that $\alpha_1{}^2 + \alpha_1{}'^2 = 1$. The operation performed by a beam splitter on the input can be expressed as,

$$\begin{bmatrix}\psi_{o1}\\ \psi_{o2}\end{bmatrix} = \begin{bmatrix}\alpha_1 & \alpha_2{}'\\ \alpha_1{}' & \alpha_2\end{bmatrix} \cdot \begin{bmatrix}A(z)\cdot\Omega_A\\ B(z)\cdot\Omega_B\end{bmatrix}, \tag{2}$$

where $T_B = \begin{bmatrix}\alpha_1 & \alpha_2{}'\\ \alpha_1{}' & \alpha_2\end{bmatrix}$ is the transfer matrix and ψ_{o1}, ψ_{o2} are outputs of the beam splitter. For a 50:50 beam splitter, power is equally distributed such that $\alpha_1 = \alpha_2 = \frac{1}{\sqrt{2}}$.

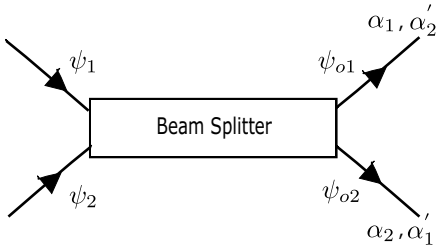

Figure 4: Beam splitter

B. Transfer matrix for a Y-splitter

A Y-splitter operates similar to a beam splitter with the difference that it takes only one input. Therefore, the transfer matrix for a Y-splitter can be derived from T_B by substituting $\alpha_2 = 0$ and input $B(z)\cdot\Omega_B = 0$ in Eqn. (2). The operation takes the form,

$$\begin{bmatrix}\psi_{o1}\\ \psi_{o2}\end{bmatrix} = \begin{bmatrix}\alpha_1\\ \alpha_1{}'\end{bmatrix} \cdot \left[A(z)\cdot\Omega_A\right], \tag{3}$$

where $T_Y = \begin{bmatrix}\alpha_1\\ \alpha_1{}'\end{bmatrix}$ is the transfer matrix and ψ_{o1}, ψ_{o2} are the outputs of Y-splitter.

C. Phase Modulator

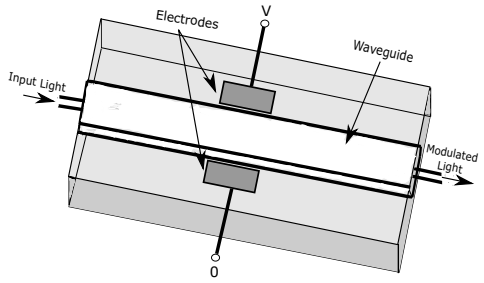

Figure 5: Phase modulation

Phase modulators, as shown in Fig. 5, are devices that modulate the phase of signal by external effects such as the thermo-optic effect, carrier injection and depletion effect, and electric field effects. Such externally affected phase changes are employed in switches and modulators. There are two efficient ways of dynamically changing the refractive index. For one, phase can be modulated by exploiting the dependency of refractive index of Si on temperature. Mathematically,

$$\Delta\phi = (\frac{2\pi}{\lambda})\Delta nL = (\frac{2\pi}{\lambda})L_h\frac{dn}{dT}\Delta T, \tag{4}$$

where $\Delta\phi$ is the phase difference, λ is the wavelength, Δn refractive index, L is optical length, L_h is the length exposed to heat and ΔT is the change in temperature. For Si, $\frac{dn}{dT}$ = 1.86×10^{-4}/K. Tungsten based heating elements are used for inducing heat. Secondly, the concentration of free charge carriers can also affect the refractive index of material as,

$$\Delta n = -\frac{e^2\lambda^2}{8\pi^2c^2\epsilon_o n}(\frac{\Delta N_e}{m^*_{ce}} + \frac{\Delta N_h}{m^*_{ch}}), \tag{5}$$

where e is the charge of electron, Δn is change in refractive index, ϵ_o is permittivity of free space, c is speed of light, n is refractive index of unperturbed crystalline-Si, ΔN_e is the change in concentration of electrons, ΔN_h the change in concentration of holes, m^*_{ch} is the conductivity effective mass of holes and m^*_{ce} the conductivity effective mass of electrons. According to Drude-Lorenz equation [15],

$$\Delta\alpha = \frac{e^3\lambda^2}{4\pi^2c^3\epsilon_o n}(\frac{\Delta N_e}{\mu_e(m^*_{ce})^2} + \frac{\Delta N_h}{\mu_h(m^*_{ch})^2}), \tag{6}$$

where $\Delta\alpha$ is change in optical absorption coefficient of Si, μ_e is the mobility of electrons, μ_h the mobility of holes. Here $\Delta\alpha$ gains positive values with increase in concentration of electrons and holes. A P-i-N diode is used to modulate signal phase by injecting or extracting carriers in a waveguide, where the waveguide itself acts as the intrinsic region.

D. Transfer matrix of Y-splitter based MZI

Mach-Zehnder Interferometer (MZI) is composed of a Y-splitter, a differential phase shift section and a Y-combiner, as shown in Fig. 6. The transfer matrix T_{MY} for an MZI can be obtained by cascading individual transfer matrices of its constituent elements.

For *propagation matrix* T_P of input waves through straight waveguides, consider two input waves $\psi_1 = A(z)\cdot\Omega_A(z)\cdot \mathrm{e}^{-i\beta_A z}$ and $\psi_2 = B(z)\cdot\Omega_B(z)\cdot\mathrm{e}^{-i\beta_B z}$, such that $\psi_1 = A(z)\cdot\Omega_A(z)\cdot\mathrm{e}^{-i\beta_A(z+z_o)}$ and $\psi_2 = B(z)\cdot\Omega_B(z)\cdot\mathrm{e}^{-i\beta_B(z+z_o)}$ after travelling a distance z_o. This transmission can be represented,

$$\begin{bmatrix}\psi_{o1}(z)\\ \psi_{o2}(z)\end{bmatrix} = \begin{bmatrix}\mathrm{e}^{-i\phi_1} & 0\\ 0 & \mathrm{e}^{-i\phi_2}\end{bmatrix}\begin{bmatrix}A(z)\\ B(z)\end{bmatrix}$$

where matrix $T_P = \begin{bmatrix}\mathrm{e}^{-i\phi_1} & 0\\ 0 & \mathrm{e}^{-i\phi_2}\end{bmatrix}$ is called propagation matrix and $\phi_1 = \beta_A(z+z_o)$ and $\phi_2 = \beta_B(z+z_o)$. The operation performed by stage I in Fig. 6 is given by Eqn. (3). Since T_Y is a 2×1 matrix and the propagation matrix for straight waveguides is a 2×2 matrix, T_Y has to be transposed in order to meet the matrix multiplication constraint. Outputs of stage II can be obtained as,

$$\begin{bmatrix}\alpha_1 A(z)\Omega_A & \alpha_1{}' A(z)\Omega_A\end{bmatrix}\begin{bmatrix}\mathrm{e}^{i\phi} & 0\\ 0 & \mathrm{e}^{-i\phi}\end{bmatrix}$$

$$= \begin{bmatrix} \alpha_1 A(z)\Omega_A e^{i\phi} & \alpha_1{}' A(z)\Omega_A e^{-i\phi} \end{bmatrix} \quad (7)$$

where $-\phi$ and ϕ are the phase shifts introduced in the upper and lower arms, respectively. By heat or carrier injection ϕ can be changed to cause constructive or destructive interference at the output, resulting in 1 or 0 signal detection, thus acting as a switch. The final output of an MZI can be obtained by multiplying the matrix obtained in stage II Eqn. (7) with the combiner's transfer matrix. Since a Y-combiner combines the inputs from its two arms (additively) and produces a single output without introducing any further phase change, stage III output T_{MY} reduces to scalar $cos(\phi)$ as shown below,

$$\begin{bmatrix} \alpha_1 A(z)\Omega_A e^{i\phi} & \alpha_1{}' A(z)\Omega_A e^{-i\phi} \end{bmatrix} \begin{bmatrix} \alpha_1 \\ \alpha_1{}' \end{bmatrix} = cos(\phi). \quad (8)$$

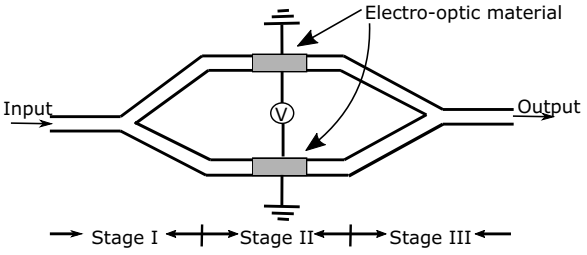

Figure 6: Y-splitter based MZI

E. Coupled mode theory

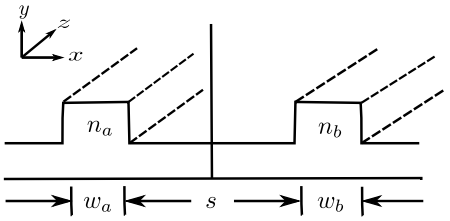

Figure 7: Cross-sectonal view of waveguide a and b

When two waveguides are in close proximity, a wave propagating in one waveguide couples into another with a phase shift of $\pi/2$. In order to compute transfer matrix for a 3dB coupler, consider two waveguides, a and b, of length L each placed in close proximity along the x-direction with refractive index n_a, n_b and width w_a, w_b, respectively. Let z be the direction of propagation and s be the spacing between the two waveguides as shown in Fig. 7. Consider a wave $\Psi(x,z)$ expressed as the linear combination of mode fields $\Omega_a(x)$ and $\Omega_b(x)$ input to the waveguides a and b. Mathematically,

$$\Psi(x,z) = A(z)\cdot\Omega_a(x)\cdot e^{-i\beta_a\cdot z} + B(z)\cdot\Omega_b(x)\cdot e^{-i\beta_b\cdot z} \quad (9)$$

Consider the equation,

$$\frac{\partial^2\Psi}{\partial x^2} + \frac{\partial^2\Psi}{\partial z^2} + \beta_o^2 n^2\Psi = 0 \quad (10)$$

derived from Helmholtz equation. Substituting Eqn. (9) in Eqn. (10) leads to coupled mode equations. For perturbed space, refractive index is expressed as follows to simplify the calculation: $n^2(x) = n_a^2(x) + \triangle n_a^2(x)$, where $\triangle n_a(x)$ is the change in refractive index experienced by wave in waveguide a while coupling into waveguide b. With coupling and orthogonality of mode fields, the differential equations of coupled waves can be written as,

$$\frac{\partial A}{\partial z} = -i\cdot\rho_{ba}B(z)\cdot e^{-i\triangle\beta\cdot z}, \frac{\partial B}{\partial z} = -i\cdot\rho_{ab}A(z)\cdot e^{-i\triangle\beta\cdot z}.$$

These are known as coupled mode equations. Solutions to these differential equations are given as,

$$\begin{aligned} A(z) &= X(z)\cdot A(0) + Y(z)\cdot B(0), \\ B(z) &= U(z)\cdot A(0) + V(z)\cdot B(0) \text{ where,} \\ X(z) &= V^*(z) = e^{\frac{-i\beta_a\cdot z}{2}}[cos(\gamma z) - \frac{i\triangle\beta}{2\gamma}sin(\gamma z)], \\ Y(z) &= (\frac{\rho_{ab}}{i\gamma})e^{\frac{-i\beta_a\cdot z}{2}}sin(\gamma z), \\ U(z) &= (\frac{\rho_{ba}}{i})\gamma e^{\frac{-i\beta_a\cdot z}{2}}sin(\gamma z), \text{ and} \\ \gamma^2 &= \frac{\triangle\beta^2}{2} + \rho^2, \rho = \sqrt{\rho_{ab}\cdot\rho_{ba}}. \end{aligned}$$

Here, ρ is the coupling coefficient. The coupled mode equations can be expressed in the matrix form as,

$$\begin{bmatrix} A(z) \\ B(z) \end{bmatrix} = \begin{bmatrix} X(z) & Y(z) \\ U(z) & V(z) \end{bmatrix} \begin{bmatrix} A(0) \\ B(0) \end{bmatrix}$$

Assuming identical waveguides, $n = n_a = n_b$, $\beta_1 = \beta_2$ ($\triangle\beta = \beta_1$-$\beta_2 = 0$), $\gamma = \rho_{ab} = \rho_{ba} = \rho$. The transfer matrix T_{MB} is

$$\begin{bmatrix} X(z) & Y(z) \\ U(z) & V(z) \end{bmatrix} = \begin{bmatrix} cos(\rho z) & -i\cdot sin(\rho z) \\ -i\cdot sin(\rho z) & cos(\rho z), \end{bmatrix} \quad (11)$$

where (ρz) represents phase ϕ of the waves. For a 3dB coupler, $\phi = \rho z = \pi/4$. Hence Eqn. (11) takes the form,

$$\begin{bmatrix} X(z) & Y(z) \\ U(z) & V(z) \end{bmatrix} = \begin{bmatrix} \frac{1}{\sqrt{2}} & -i\cdot\frac{1}{\sqrt{2}} \\ -i\cdot\frac{1}{\sqrt{2}} & \frac{1}{\sqrt{2}} \end{bmatrix}. \quad (12)$$

F. Transfer matrix for 3dB coupler based MZI

A 3dB coupler based MZI is constructed by using 3dB couplers and phase modulators as shown in Fig. 8. The transfer matrix T_{MC} of such MZI can be obtained by multiplication of transfer matrices of constituent elements.

$$T_{MC} = \frac{1}{2}\begin{bmatrix} 1 & -i \\ -i & 1 \end{bmatrix} \begin{bmatrix} e^{-i\phi_1} & 0 \\ 0 & e^{-i\phi_2} \end{bmatrix} \begin{bmatrix} 1 & -i \\ -i & 1 \end{bmatrix} \quad (13)$$

$$T_{MC} = \frac{1}{2}\begin{bmatrix} e^{-i\phi_1} - e^{-i\phi_2} & -i(e^{-i\phi_1} + e^{-i\phi_2}) \\ -i(e^{-i\phi_1} + e^{-i\phi_2}) & -e^{-i\phi_1} + e^{-i\phi_2} \end{bmatrix} \quad (14)$$

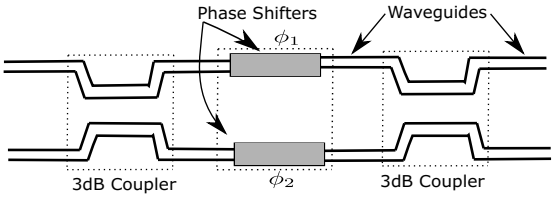

Figure 8: Mach Zehnder interferometer

IV. Model abstraction from experiments

The OEIC design suite of tools provided by Ansys Lumerical enables the design of photonic components and circuits [8]. It provides a framework for physical device design, analysis and simulation engines based on eigen solving and FDTD numerical computations for performance analysis of optical design components. We used this suite to analyze the behavior of devices in presence of geometric and layout variations, and derive abstraction models from these experiments.

A. Y-splitter

An ideal Y-splitter, as shown in Fig 9, has equal power and no phase difference at the two output arms. Simulations for a prototype component are performed in varFDTD to analyze the effect of physical deformity at the output parameters. Deformities are introduced by dislocating the lower arm from its ideal position. Simulations are performed for dislocations starting from 0 to 450 nm with a step size of 50nm. It can be observed from Table I that there is no phase difference for the ideal Y-splitter arms. However, the disfigured geometry shown in Fig. 10 introduces a phase difference $(\Delta\phi)$ among the arms, and also leads to redistribution of transmitted power in upper (T_{xu}) and lower arms (T_{xl}).

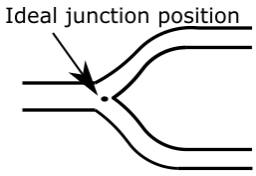

Figure 9: Ideal Y-Splitter

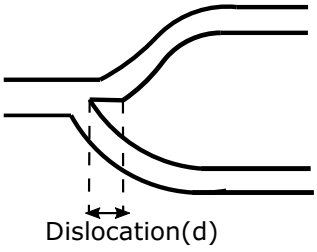

Figure 10: Deformed Y-Splitter

Model abstraction aims to develop analytical compact models to predict the behavior of a component in the presence of such design errors or manufacturing induced deformity. Polynomial equations are obtained by curve fitting the data obtained in Table I to characterize the behavioral effects of such a deformity. These equations are a function of dislocation such that they predict the change in phase and transmitted power for a given value of dislocation when incorporarated into corresponding transfer matrices. The scaling factor for transmitted power in upper and lower arms of a deformed Y-splitter are Δ_{UY} and Δ_{LY}, respectively, and are computed to be,

Table I: Effect of deformity on power and phase in a Y-splitter simulated using varFDTD

Dislocation d (μm)	Tx_U	Tx_L	$\Delta\phi(rad)$	Comp. time (sec)
0	0.47	0.47	0	9.64
0.05	0.466	0.468	0.027	9.723
0.1	0.463	0.471	0.035	8.68
0.15	0.459	0.475	0.098	8.69
0.2	0.469	0.479	0.137	8.70
0.25	0.464	0.483	0.18	8.69
0.3	0.461	0.482	0.235	8.73
0.35	0.456	0.486	0.371	8.82
0.4	0.458	0.491	0.324	8.68
0.45	0.453	0.493	0.372	10.11

$$\Delta_{LY} = 0.6649964 - 0.2400577 \cdot d + 4.315981 \cdot d^2 - \\ - 22.31828 \cdot d^3 + 49.46869 \cdot d^4 - 39.45889 \cdot d^5 \quad (15)$$

$$\Delta_{UY} = 0.6655622 - 0.2804852 \cdot d + 2.48959 \cdot d^2 - \\ 8.509644 \cdot d^3 + 10.41863 \cdot d^4 - 2.901393 \cdot d^5 \quad (16)$$

where d is dislocation (in μm) of lower arm from its ideal position. Substituting Eqn. (15) and Eqn. (16) in Eqn. (3),

$$\begin{bmatrix}\psi_{o1}\\ \psi_{o2}\end{bmatrix} = \begin{bmatrix}\alpha_1 \cdot \Delta_{UY}\\ \alpha_1^{'} \cdot \Delta_{LY}\end{bmatrix} \cdot \big[A(z) \cdot \Omega_A\big] \quad (17)$$

It can be computed from Eqn. (17) that ψ_{o1} = ψ_{o2} = 0.47 when d = 0. We perform similar abstractions to observe the effect of deformity d on the phase of signal on both Y-splitter arms. Assuming ϕ_2, ϕ_1 as phase of the signal in lower arm and upper arm respectively, the phase difference introduced between the two arms, $\Delta\phi$, is obtained and expressed as,

$$\Delta\phi = -0.0007342657 + 0.7467832 \cdot d - 6.546387 \cdot d^2 - \\ 49.50816 \cdot d^3 - 109.2774 \cdot d^4 + 71.79487 \cdot d^5 \quad (18)$$

where $\Delta\phi$ = ϕ_2-ϕ_1. The phase difference gained by two outputs can be computed as $m \cdot \phi$, where m is the number of cascaded stages. In order to analyze the impact of this fabrication defect, Y-splitters are cascaded together as shown in Fig. (11). Such Y-splitters are used in $1 : n$ multiplexers and for signal sharing fanouts in optical circuits. Y-splitters are also constituent elements of MZIs, and long chains of such MZIs are used in optical neural network, optical logic and for pulse transmission.

Simulation is performed in FDTD to analyze the effect of deformities on transmitted power T_x and phase ϕ. Results tabulated in Table II show transmitted power in the ideal case T_{xI}, transmitted power in deformed case T_{xd}, transmitted power calculated using our mathematical model T_{xc}, and computation time for simulation in respective cases. Ideally, there is no phase difference between the two outputs of a Y-splitter. We performed experiment where the 1^{st} stage Y-splitter and lower Y-splitter of 2^{nd} stage are deformed. Our model shows that a

Table II: Effect of deformity on power and phase in cascaded two stage Y-splitters

Component	T_{xI}	T_{xd}	T_{xc}
Arm 1	0.465	0.466	0.459
Arm 2	0.478	0.485	0.493
Arm 3	0.202	0.0.208	0.210
Arm 4	0.208	0.203	0.226
Arm 5	0.215	0.209	0.226
Arm 6	0.205	0.226	0.243
Computation time (sec)	1900.09	1930.11	0.0026

phase difference of 0.204 rad is developed after two cascaded stages, which is verified by FDTD simulation result of 0.22 rad. However, computation time for our model (0.0026sec) is orders of magnitude smaller than for FDTD simulation (1930.11sec).

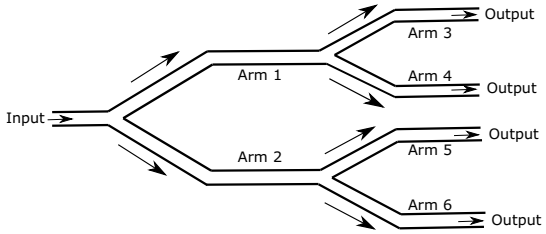

Figure 11: Cascaded Y-splitter

B. 3dB coupler

A 3dB coupler divides input power equally into two arms with the coupled wave phase shifted (lag) by $\pi/2$. Couplers may have non-ideal coupling lengths and spacing between straight waveguides, resulting due to fabrication defects. Simulations for a prototype 3dB coupler are performed in varFDTD with coupling length L_c= 23μm and gap s = 0.25μm. Then, spacing between the straight waveguides section is varied from 0.25μm to 0.30μm with a step size of 0.05μm. It can be observed from Table III that in the presence of deformity a 3dB coupler may behave as a 70:30 coupler, and the phase difference $\Delta\phi$ among output arms changes abruptly from $-\frac{3\pi}{2}$ to $\frac{\pi}{2}$ for 15 to 20nm of dislocation. It is observed that a 3dB coupler is fairly tolerant to any change in spacing between waveguides for 0-15nm or 20-55nm.

The scaling factor for transmitted power in upper and lower arms of a deformed 3dB coupler are Δ_{UC} and Δ_{LC}, respectively, and were computed by curve fitting Table III,

$$\Delta_{UC} = 0.6930792 + 9.170137 \cdot s - 194.4096 \cdot s^2 + 7787.592 \cdot s^3 - 157598.2 \cdot s^4 + 1160556 \cdot s^5 \quad (19)$$

$$\Delta_{LC} = 0.6931337 - 9.781455 \cdot s + 338.3219 \cdot s^2 - - 16196.51 \cdot s^3 + 350797.7 \cdot s^4 - 2701193 \cdot s^5, \quad (20)$$

Table III: Effect of non-ideal spacing between waveguides on power and phase in a 3dB coupler as simulated by varFDTD

Dislocation s (μm)	Tx_U	Tx_L	$\Delta\phi(rad)$	Comp. time (sec)
0	0.49	0.49	-4.7	205.119
0.005	0.52	0.46	-4.699	195.54
0.01	0.544	0.437	-4.698	151.101
0.015	0.572	0.410	-4.7	197.2
0.02	0.593	0.391	1.581	149.382
0.025	0.616	0.366	1.581	143.355
0.035	0.639	0.343	1.58	140.635
0.04	0.661	0.322	1.578	183.417
0.045	0.681	0.302	1.579	255.979
0.05	0.699	0.285	1.578	1.579
0.055	0.719	0.264	1.578	101.794

where spacing s is as shown in Fig. 7. Substituting Eqn. (19) and Eqn. (20) in Eqn. (12),

$$T_{MB} = \begin{bmatrix} \frac{1}{\sqrt{2}} \cdot \Delta_{UC} & -i \cdot \frac{1}{\sqrt{2}} \cdot \Delta_{LC} \\ -i \cdot \frac{1}{\sqrt{2}} & \frac{1}{\sqrt{2}} \end{bmatrix} \quad (21)$$

Since a 3dB coupler is one of the constituent elements of MZI, a deformed 3dB coupler can effect the output of MZI. Substituting Eqn. (21) in Eqn. (13) transfer matrix for deformed MZI is obtained below.

$$T_{MC} = \frac{1}{2} \begin{bmatrix} \Delta_{UC} & -i\Delta_{LC} \\ -i & 1 \end{bmatrix} \begin{bmatrix} \mathrm{e}^{-i\phi_1} & 0 \\ 0 & \mathrm{e}^{-i\phi_2} \end{bmatrix} \begin{bmatrix} 1 & -i \\ -i & 1 \end{bmatrix}$$

In another experiment, we introduced coupling length L_c deformity by changing the length of lower straight waveguide. Simulations are performed in varFDTD by varying the length L_c from 23 to 23.50μm with a step size of 50nm. It can be observed from Table IV that a 3dB coupler with non-ideal coupling length experiences a change in phase difference but almost no change in power distribution at the output arms. The scaling factors $\Delta\phi_u$, $\Delta\phi_l$ for change in phase shift in upper and lower arm are computed from Table IV,

$$\Delta\phi_u = -0.499986 - 0.02159674 \cdot L + 0.01177156 \cdot L^2 + 0.01398601 \cdot L^3 - 0.04662005 \cdot L^4 - 1.961808 \times 10^{14} \cdot L^5, \quad (22)$$

$$\Delta\phi_l = -4.30149 + 108.2905 \cdot L - 1696.644 \cdot L^2 + 10139.44 \cdot L^3 - 23951.66 \cdot L^4 + 19405.13 \cdot L^5, \quad (23)$$

where L is deviation in coupling length. Transfer matrix of MZI comprising a deformed 3dB coupler can be computed by substituting Eqn. (23) in Eqn. (13),

$$T_{MC} = \frac{1}{2} \begin{bmatrix} 1 & -i \\ -i & 1 \end{bmatrix} \begin{bmatrix} \mathrm{e}^{-i\Delta\phi_u} & 0 \\ 0 & \mathrm{e}^{-i\Delta\phi_l} \end{bmatrix} \begin{bmatrix} 1 & -i \\ -i & 1 \end{bmatrix}.$$

V. Application of our model on logic circuit

We demonstrate the application of our model to analyze the effect of a deformity in an optical digital logic circuit. Using the optical logic synthesis methodology of [5], logic

Table IV: Effect of non-ideal coupling length on power and phase in a 3dB coupler as simulated by varFDTD

Dislocation L (μm)	Tx_U	Tx_L	Phase upper arm (rad)	Phase lower arm (rad)	Comp. time (sec)
0	0.49	0.49	-0.500	-5.200	205.119
0.05	0.50	0.47	-0.501	1.153	101.959
0.1	0.5	0.482	-0.502	-5.045	102.209
0.15	0.501	0.483	-0.503	-4.927	107.812
0.2	0.500	0.484	-0.504	1.423	156.146
0.25	0.501	0.485	-0.504	1.533	148.203
0.3	0.499	0.486	-0.506	1.665	101.637
0.35	0.500	0.488	-0.506	1.754	104.213
0.40	0.501	0.487	-0.507	1.853	104.745
0.45	0.501	0.487	-0.508	1.954	99.185
0.5	0.503	0.485	-0.509	2.084	100.99

functions are composed of 2×2 electrically controlled optical crossbar gates implemented using 3dB coupler based MZIs. As depicted in Figs. 12-14, the switching input S is an electrical input, P, Q are optical inputs and F, G optical outputs, where S modulates/switches the device into a cross or a bar configuration. Signal $S = 1$ introduces a phase shift of $\Delta\phi = 0$ in the modulating arms, whereas $S = 0 \implies \Delta\phi = \pi$. The waveguides are sourced by light (logic "1") or darkness ("0"), and the function is photo-detected at the output.

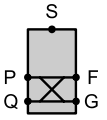

Figure 12: Gate

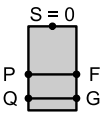

Figure 13: Bar

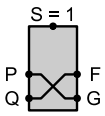

Figure 14: Cross

Fig. 15 implements a Boolean function corresponding to Segment-0 of a BCD-to-7segment display using 5 MZIs. Consider the input $X_3X_2X_1X_0 = 0100$ (decimal digit 4) which should set Segment-0 to "0". In our experiment, we introduce a deformed MZI at the device controlled by X_0. Under the above input, the deformity couples light in both arms of the MZI controlled by X_0. Simulation of this circuit by FDTD or mode solvers is infeasible. However, using our method, simulation was performed in 0.1025 seconds in Python. We read the netlist, and compose the transfer matrices for each device, incorporating the abstracted scaling factors for the deformed device. Our simulation estimates that more than 30% power is detected at Segment-0, which is detected as logic 1.

Our model further estimates a phase shift of $\Delta\phi = 2.4$ rad at the MZI controlled by X_0, instead of the ideal case of 3.14 rad. Our approach can further assist in *post-fabrication tuning to rectify the effect of this deformity*. We use the relation $\phi = \frac{2\pi eVL}{D\lambda}$, where e is the electro-optic coefficient of the medium, V the voltage applied to the phase modulator, L the length of the electro-optic section, D the distance between electrodes, to estimate that an external voltage of -0.6 V on the lower arm (Fig. 8) compensates for the imperfect coupling and provides a 0.6 (strong "1" detection) and 0.06 (strong "0" detection) transmission at the segment-0 output.

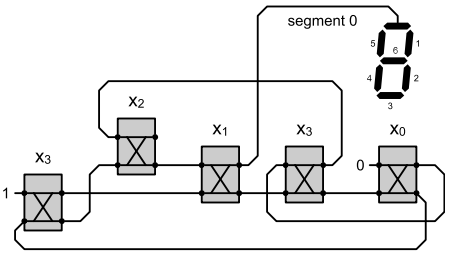

Figure 15: Segment "0" of BCD-to-7 Segment Display

VI. Conclusion

This paper has proposed an abstraction model to evaluate the effect of manufacturing process variations in linear optical devices. Experiments are performed to analyze the behavior of devices under geometric and layout variations, designed with conventional SOI waveguides. The results are curve fitted into a compact model and incorporated into transfer matrix representations of devices. The models are constructed to observe the impact of deformities on power transmission and phase in OEICs. Our approach is demonstrated by application on a optical logic circuit which includes a deformed device. It is shown that our models can also help with post-fabrication tuning of OEICs impacted by manufacturing variations. As future work, we are researching analogous models for resonance-based devices, and testability metrics for Si-photonics.

References

[1] A. Politi, J. C. Matthews, and J. L. O'Brien, "Shor's quantum factoring algorithm on a photonic chip," *Science*, vol. 325, no. 5945, pp. 1221–1221, 2009.

[2] A. J. Poustie and K. J. Blow, "Demonstation of an all-optical fredkin gate," *Optics Communications*, vol. 174, pp. 317–320, 2000.

[3] S. Kotiyal and et al., "Mach-zehender interferometer based design of all optical reversible binary adder," in *Proc. Des. Auto. Test Europe (DATE)*, 2012, pp. 721–726.

[4] Y. Shen and *et al.*, "Deep learning with coherent nanophotonic circuits," *Nature Photonics*, vol. 11, no. 441-446, 2017.

[5] C. Condrat, P. Kalla, and S. Blair, "Logic synthesis for integrated optics," in *Proc. Great Lakes Symp. VLSI*. ACM, 2011, pp. 13–18.

[6] A. Qouneh, Z. Li, M. Joshi, W. Zhang, X. Fu, and T. Li, "Aurora: A thermally resilient photonic network-on-chip architecture," in *IEEE Intl. Conf. Computer Design (ICCD)*. IEEE, 2012, pp. 379–386.

[7] L. Chrostowski and M. Hochberg, *Silicon Photonics Design: From Devices to Systems*. Cambridge University Press, 2015.

[8] *Lumerical Photonic Design Software*, Lumerical Computational Solutions, Inc., www.lumerical.com.

[9] F. Bucholtz and J. Singley, "Matrix representations for classical and quantum beam splitters," *Optical Engineering*, vol. 59, no. 12, pp. 1–13, 2020.

[10] C. Chang, "Discrete-sample curve fitting using Chebyshev polynomials and the approximate determinations of optimal trajectories via dynamic programming," *IEEE Trans. Auto. Control*, vol. 11, no. 1, 1966.

[11] J. De Coster, "Test-station for flexible semi-automatic wafer-level silicon photonics testing," in *Proc. Eur. Test Symp.*, 2016, pp. 1–6.

[12] L. Chrostowski and *et al*, "Impact of fabrication non-uniformity on chip-scale silicon photonic integrated circuits," in *Optical Fiber Communication Conference*. Optical Society of America, 2014, pp. Th2A–37.

[13] M. Nikdast, G. Nicolescu, J. Trajkovic, and O. Liboiron-Ladouceur, "Chip-scale silicon photonic interconnects: A formal study on fabrication non-uniformity," *Journal of Lightwave Technology*, vol. 34, no. 16, pp. 3682–3695, 2016.

[14] S. Banerjee, M. Nikdast, and K. Chakrabarty, "On the impact of uncertainties in silicon-photonic neural networks," *IEEE Design & Test (early access), DOI: 10.1109/MDAT.2022.3161599*, 2022.
[15] R. A. Soref and B. Bennett, "Electrooptical effects in silicon," *Quantum Electronics, IEEE Journal of*, vol. 23, no. 1, pp. 123–129, 1987.